Inhomogeneous extragalactic magnetic fields and the second knee in the cosmic ray spectrum

Kumiko Kotera, Martin Lemoine

Inhomogeneous extragalactic magnetic fields and the second knee in the cosmic ray spectrum

Kumiko Kotera* and Martin Lemoine†

Institut d'Astrophysique de Paris UMR7095 - CNRS, Université Pierre & Marie Curie, 98 bis boulevard Arago F-75014 Paris, France

(Received 8 June 2007; published 28 January 2008)

Various experiments indicate the existence of a second knee around energy $E = 3 \times 10^{17}$ eV in the cosmic ray spectrum. This feature could be the signature of the end of the galactic component and of the emergence of the extragalactic one, provided that the latter cuts off at low energies. Recent analytical calculations have shown that this cutoff could be a consequence of the existence of extragalactic magnetic fields (Refs. [M. Lemoine, Phys. Rev. D **71**, 083007 (2005).][R. Aloisio and V. Berezinsky, Astrophys. J. **625**, 249 (2005).]): low energy protons diffuse on extragalactic magnetic fields and cannot reach the observer within a given time. We study the influence of inhomogeneous magnetic fields on the magnetic horizon, using a new semianalytical propagation code. Our results indicate that, at a fixed value of the volume averaged magnetic field $\langle B \rangle$, the amplitude of the low energy cutoff is mainly controlled by the strength of magnetic fields in the voids of the large-scale structure distribution.

DOI: 10.1103/PhysRevD.77.023005 PACS numbers: 98.70.Sa, 98.62.En, 98.65.Dx

I. INTRODUCTION

Recent developments in our understanding of the origin of cosmic rays have led to the suggestion that the cosmic ray spectrum might comprise only two components, one of galactic origin, dominant in the energy range $E \lesssim 10^{17}$ eV, and another of extragalactic origin in the energy range $E \gtrsim 10^{18}$ eV [1]. In this interpretation, the crossover between the two components marks the so-called ''second knee'' in the all particle cosmic ray spectrum (see Ref. [2] for a review on cosmic ray data at high energies), while the ''first knee'' at $E \sim 2 \times 10^{15}$ eV would be associated with a change of propagation regime or the maximal energy of protons at the source. The third feature in the cosmic ray spectrum, i.e., the ''ankle'' at $E \sim 10^{19}$ eV would be a consequence of pair production losses of ultrahigh energy protons accelerated in sources located at cosmological distances [1].

On purely phenomenological grounds, this modern view is appealing when compared to the more traditional interpretation in which the ankle is associated with the emergence of an extragalactic cosmic ray component out of a more steeply falling spectrum at energies $E \lesssim 10^{19}$ eV. One of these major advantages certainly is the ''economy'' of sources. It is indeed notoriously difficult to accelerate particles beyond $E \approx 10^{15}$ eV in supernovae remnants [3]. Therefore, if the first knee corresponds to the maximal energy of protons at the source, the falloff of the galactic component at $\sim 10^{17}$ eV would naturally be associated with the maximal energy of the iron component at the source. On the contrary, if the extragalactic component appears at the ankle, one needs to postulate the existence of a third cosmic ray component between $\sim 10^{17}$ eV and $\sim 10^{19}$ eV (see for instance Ref. [4] for a recent proposal), or to assume that supernovae are able to accelerate particles up to the ankle (see for instance [5]).

The modern interpretation of a transition between the galactic and the extragalactic component at the second knee does not come without flaws, however. In particular, the smooth matching of the galactic and extragalactic components at $E \sim 10^{17}$ eV bears the unaesthetic look of fine-tuning. Of course, this problem is generic to the matching of two distinct components at a point where the slope steepens; the introduction of a third cosmic ray component would not help in this respect. As far as the galactic component is concerned, the falloff at $E \gtrsim 10^{17}$ eV arises as a direct consequence of the observation of the first knee, as mentioned above. However one must explain why the extragalactic component vanishes at energies below the second knee. In the original scenario of Berezinsky *et al.* [1], this low energy cutoff was attributed to physics at the source. In Ref. [6], it was suggested to interpret it as the modulation of the extragalactic flux due to a galactic magnetized wind, although the calculations of Ref. [7] bring down this cutoff to a too low energy, $E \sim 10^{15}$–10^{16} eV.

Another possibility, advocated in Refs. [8,9] is to relate this cutoff with the influence of extragalactic magnetic fields. As demonstrated in these studies, if the intensity of extragalactic magnetic fields is rather modest, say $\langle B \rangle \sim 10^{-9}$ G, the diffusion time of particles with energy $E \lesssim 10^{17}$ eV from the closest sources (located at, say $\sim$50–100 Mpc) becomes longer than the age of the Universe. This produces a low energy cutoff in the propagated spectrum at the required location, which allows to reproduce a smooth transition at the second knee in agreement with observational data (see [8]).

It has also been argued that if ultrahigh energy cosmic rays comprised a significant fraction of heavy nuclei ($\gtrsim$ 20%), the scenario of a transition at the second knee would loose its merits as the energy losses would no longer be able to reproduce the ankle feature [10,11]. However even a solar type (or galactic cosmic ray type) chemical composition, with $\sim$10% helium and only traces of heavier elements, allows to fit the existing data at the ankle with a

*kotera@iap.fr
†lemoine@iap.fr

single powerlaw spectrum at injection [1]. Furthermore, there is no particular reason to expect the source composition to be enriched in metals. In any case, future measurements of the chemical composition will tell [10,12].

Quantizing the influence of extragalactic magnetic fields on the spectrum of cosmic rays with energy $E \sim 10^{17}$ eV is not an easy task as the propagation times become of the order of a Hubble time, hence one must account for the effects of expansion. For the sake of simplicity, Refs. [8,9] have thus assumed the magnetic field power to be distributed homogeneously in space. However, this approximation deserves to be refined since the magnetic field is most likely distributed as the charged baryonic plasma. Since the scale of inhomogeneity of large-scale structure in the Universe is comparable to the distance to the closest sources, ~50–100 Mpc, the inhomogeneity of the magnetic field may affect the conclusions of Refs. [8,9]. The objective of the present paper is precisely to address this issue and to study the scenario put forward in these references in a more realistic extragalactic magnetic field configuration.

This immediately brings forward the difficulty of defining a realistic distribution of large-scale extragalactic magnetic fields, including the shape and amplitude of a turbulent magnetic cascade. From an observational point of view, one has been able to measure the strength of extragalactic magnetic fields ''only'' in the core of clusters of galaxies [13]; a bridge of synchrotron emission on Mpc scales has been observed in the Coma cluster [14]. Hopefully the SKA project will enlarge considerably the data set on extragalactic magnetic fields [15] but it is not expected to enter operation before 2017. In the meantime, one thus has to rely on theory. Unfortunately, the very origin of extragalactic magnetic fields is unknown, see Ref. [16] for a review. Furthermore, even if one knew exactly the initial conditions that set the configuration of magnetic fields at a high redshift, the simulation of their evolution throughout cosmic history to the present, carrying sufficient accuracy on a large dynamic range of spatial scales, remains a formidable task for numerical computing.

In regards of all these uncertainties on the origin of extragalactic magnetic fields, on their distribution in the present Universe, on the nature and shape of magnetic turbulence as well as on the transport properties of particles in chaotic magnetic fields, we adopt a simplified and parametrized description which allows us to evaluate the effects of the various sources of uncertainties on the results. As a by-product of the present study, we thus propose a simple and new recipe to build semirealistic magnetic field distributions out of dark matter simulations (which can be obtained at a lesser cost than MHD numerical simulations) as well as a new transport scheme which is more efficient than existing codes in several respects. In particular, it allows to enlarge artificially the range of scales on which the magnetic field is distributed, hence to model the influence of intergalactic magnetized turbulence on particle transport. These techniques, which are developed in Sec. II and in Appendix A, allow us to bracket the possible distributions of extragalactic magnetic fields at the present time and their impact on the ultrahigh energy cosmic ray spectrum. Our results indicate that, at a fixed value of the volume averaged $\langle B \rangle$, the amplitude of the low energy cutoff is controlled by the strength $B_{\rm void}$ of magnetic fields in the voids of the large structure distribution and the source distance scale $n_s^{-1/3} = 50$ Mpc. The fact that our conclusions depend more weakly on other parameters characterizing the magnetic field distribution provides an adequate *a posteriori* justification for our semianalytic construction. We also argue that this simulation technique offers various advantages over existing full-blown MHD simulations of large-scale structure formation, at least as far as cosmic ray propagation is concerned.

The paper is organized as follows. In Sec. II, we present our scheme of inhomogeneous magnetic field simulation and the numerical technique of cosmic ray transport. We compare these techniques to existing simulations and discuss the advantages and drawbacks of each. In Sec. III we address the issue of the low energy cutoff in various models of extragalactic magnetic fields distributions, compute the spectra and compare them to experimental data. Section IV discusses the limitations of our approach and possible future avenues of research. Finally, Sec. V summarizes our findings.

II. PROPAGATION OF HIGH ENERGY COSMIC RAYS IN EXTRAGALACTIC MAGNETIC FIELDS

The straightforward way to study the influence of extragalactic magnetic fields boils down to performing Monte Carlo simulations of particle propagation in a simulated magnetized universe. This, however, brings in two major difficulties, which were alluded to earlier but which are rarely discussed in the literature: *(i)* an accurate numerical modeling of the transport of charged particles in magnetic fields; *(ii)* an accurate numerical modeling of the magnetized volume, including magnetized turbulence.

Point *(i)* deals with the theory of cosmic ray diffusion, which in spite of a long history and recent major progress, has not yet reached a consensus on the transport of cosmic rays in MHD turbulence (see Ref. [17] for a recent review). Actually, the simulation of particle transport in a well-defined MHD environment is not trivial even from a purely numerical point of view. For example, Ref. [18] has demonstrated that the interpolation of the magnetic field from a numerical grid gives an erroneous description of particle transport if the Larmor radius $r_L \lesssim l_{\rm min}$, where $l_{\rm min}$ represents the grid size, i.e., the minimum scale of the turbulence inertial range. Point *(ii)* deals with the problem of simulating realistic MHD flows on a large range of spatial scales, which also constitutes a field of research in its own right.

A. Magnetic field modeling

Several pioneering works have studied the propagation of cosmic rays in so-called "realistic" magnetized environments [19–21]. These studies have constructed the magnetized cube out of a hydrodynamical simulation of large-scale structure formation, which follows the magnetic field in a passive way for Ref. [21], and with feedback effects on the matter evolution for Ref. [20]. The initial conditions for this magnetic field have been set at a high redshift (although Ref. [21] also models the production of magnetic fields at accretion shock waves) and the overall amplitude of this field has been rescaled at the end of the simulation so as to reproduce the observed strength of magnetic fields in the core of clusters of galaxies. This ingenious procedure allows one to fix the volume averaged magnetic field independently of the origin of the magnetic field, although the volume averaged magnetic field now depends on the details of the amplification process during cluster formation.

In Ref. [21], the authors follow the trajectory of cosmic rays using Monte Carlo methods while the authors of Ref. [19] derive an upper bound on the typical cosmic ray deflection using a semianalytic transport scheme. Their conclusions are radically different: the former authors derive a typical deflection of $\sim 10°$–$20°$ above 10^{20} eV while the latter finds a deflection less than a degree at these energies. This discrepancy illustrates the inherent complexity of such simulations. The complexity and the cost of such numerical simulations are such that it has not been possible to elucidate the precise origin of this discrepancy yet. It is likely that most of this difference is to be attributed to the modeling of the extragalactic magnetic field, and to a lesser degree, to the transport scheme.

Figure 1, which presents the volume filling factors of the magnetic field strength obtained in these numerical simulations is particularly instructive (the model of Ref. [19] is shown as the dot-dashed line, while the model of Ref. [21] is given by the long-dashed line). It reveals large differences in the volume averaged magnetic field as well as in the spatial distribution of these fields (which translates in this figure as a difference in the slopes of the volume filling factor). Again, the origin of this difference is not understood. This figure clearly demonstrates that *the simulated magnetized volumes, despite all the sophistication of the numerical codes used, cannot truly be deemed as realistic*. It also indicates the need for alternative methods to study the transport of high energy cosmic rays in extragalactic magnetic fields, in order to provide new angles of attack on this difficult problem. This constitutes one major motivation of the present work, in which we develop one such method and apply it to the study of the low energy cutoff at energies close to the second knee.

Our magnetized volume is constructed in a simple way as compared to Refs. [19,21], this simplicity offering various advantages (and admittedly, several drawbacks) as

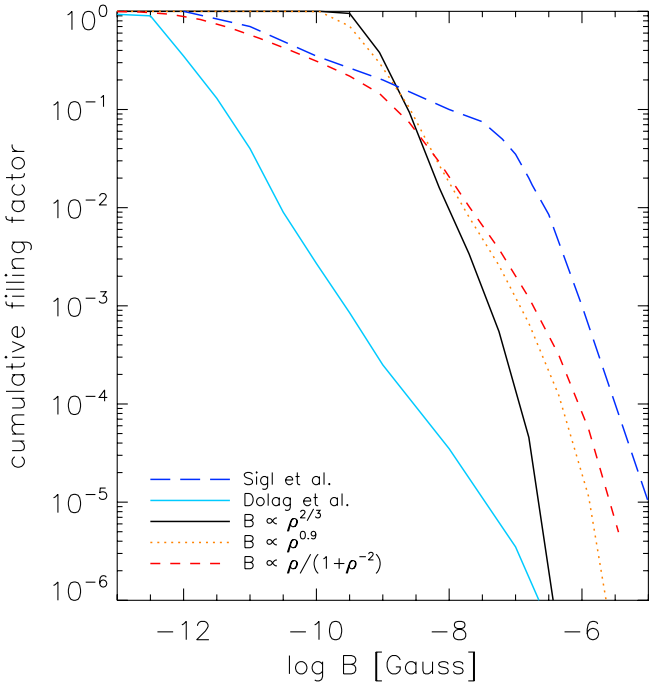

FIG. 1 (color online). Volume filling factor of the magnetic field in different scenarios. In dot-dashed line, the magnetic field simulated by Dolag and coauthors in Ref. [19]; in long-dashed line, that simulated by Sigl and coauthors [21]. In solid line, the semianalytic model with $B \propto \rho^{2/3}$, in orange dotted line, $B \propto \rho$. In (red) dashed lines, the model $B \propto \rho[1 + (\rho/\bar{\rho})^{-2}]$; this model simulates a volume with unmagnetized voids. In all cases the proportionality factor $B_0 = 2$ nG.

discussed further below. The core of our method is to map the magnetic field strength over the gas density using an analytical relation $B(\rho)$ (to be specified later) and to distribute randomly the magnetic field orientation in cells of coherence length l_c. The gas density itself is obtained from a high resolution dark matter numerical simulation of large-scale structure formation (with standard cosmological parameters $\Omega_\Lambda = 0.7$, $\Omega_m = 0.3$, and $H_0 = 70$ km/s/Mpc). Once the volume has been set up, cosmic ray trajectories are simulated as follows. At each step, the cosmic ray is supposed to enter a spherical cell of coherence of the magnetic field defined by its diameter l_c, in which the magnetic field orientation is random. The time spent in the cell and the direction of exit of the cosmic ray are then drawn from semianalytic distributions which simulate the transport of the particle in MHD turbulence, according to studies carried out in Refs. [18,22] (see Appendix A for a detailed discussion). The particle is then moved to another coherent cell and the next step is simulated. As we explain in Sec. III B, we finally compute the propagated spectrum in the low energy region $E \lesssim 10^{17}$ eV in a semianalytic way which allows us to model the effect of cosmological expansion over the course of propagation from the source to the detector. In detail, we use the Monte Carlo simulations of particle propagation in

the extragalactic magnetic fields at zero redshift in order to measure the diffusion coefficients, and use existing analytical formulas in order to calculate the propagated spectra from the diffusion equation in an expanding space-time. More details on this latter step are provided in Sec. III B.

Note that the density field of dark matter provides a good approximation to that of the gas density in the intergalactic medium (IGM) on scales larger than a few hundred kpc, corresponding to the baryon Jeans length. Therefore the overall baryonic gas density field can be obtained by smoothing the dark matter distribution by a window function of this size. Our dark matter simulation, run with the hydrodynamical code RAMSES [23], is 512^3, with extent 280 Mpc, hence with a grid size $\simeq 560$ kpc: in this case the minimum scale of the simulation then plays the role of the window function and no smoothing is required. Of course, this treatment does not provide a perfect description of the gas distribution but we have checked that decreasing the resolution by a factor 2 does not affect our results. Moreover the gas density field serves only as a marker of the magnetic field distribution, so that the above error is negligible in comparison to the uncertainty surrounding the strength and configuration of the magnetic field. The essential is rather the law $B(\rho)$ which provides the mapping between the magnetized volume and the density field.

In the case of isotropic collapse, it is well-known that $B \propto \rho^{2/3}$ in a plasma of infinite conductivity. This law is slightly oversimplistic because it ignores the anisotropy of collapse in large-scale structures, which results in an enhanced amplification of the magnetic field by shear and anisotropic compressive flows [24]. In detail, the equations of ideal MHD lead to the conservation law:

$$\frac{\mathrm{d}}{\mathrm{d}t}\left(\frac{\mathbf{B}}{\rho}\right) = \left(\frac{\mathbf{B}}{\rho}\cdot\nabla\right)\mathbf{v}, \tag{1}$$

which allows to derive the magnification of $\mathbf{B}$ from the deformation of the density field. If the separation $\delta\mathbf{q}^<$ between two points is mapped into $\delta\mathbf{q}^> = \mathcal{D}\cdot\delta\mathbf{q}^<$ through deformation, where $\mathcal{D}$ indicates the deformation tensor, then $\mathbf{B}^</\rho^<$ is mapped into $\mathcal{D}\cdot\mathbf{B}^</\rho^<$, so that:

$$\frac{B^>}{B^<} = \frac{\rho^>}{\rho^<}\frac{|\mathcal{D}\cdot\mathbf{B}^<|}{B^<}. \tag{2}$$

From Eq. (2), it is then easy to derive the law $B \propto \rho^{2/3}$ for isotropic collapse, or $B \propto \rho$ for anisotropic collapse along one (i.e., collapse on a wall) or two (i.e., collapse on a filament) spatial directions. The law $B \propto \rho^{0.9}$ has indeed been observed in the simulations of Dolag and coauthors [19].

Viscosity and shear flows during collapse may also amplify further the magnetic field, leading to departures from the law $B \propto \rho$ between regions of very different density, in particular, the voids and the structures (filaments and pancakes). For instance both simulations of Refs. [19,21] lead to weaker values of the magnetic fields in the voids than would be expected from an extrapolation of the law $B \propto \rho$ to regions of low density. In order to bracket these different effects, we consider several relations $B(\rho)$:

$$B \propto \rho^{2/3}, \tag{3}$$

$$B \propto \rho^{0.9}, \tag{4}$$

$$B \propto \rho\left[1 + \left(\frac{\rho}{\langle\rho\rangle}\right)^{-2}\right]. \tag{5}$$

The last model is an *ad hoc* modeling of the suppression of magnetic fields in the voids of large structure which leaves unchanged the distribution in the dense intergalactic medium (meaning $\rho > \langle\rho\rangle$).

B. Why a semianalytical propagation method?

At this stage, one should compare the respective merits and drawbacks of this new method with other existing techniques. Concerning the magnetic field distribution, our method obviously neglects subtle effects such as the amplification of the magnetic field in the vicinity of accretion shock waves of large-scale structure. However, it should be clear that no numerical simulation can claim to simulate with accuracy the magnetic field in the vinicity of cosmological shock waves due to the intricacy of MHD physics at play. The amount of amplification, the coherence length and the shape of the turbulence spectrum remain open questions (see however [25] for a detailed discussion of the Weibel instability operating at intergalactic shocks).

By considering a one-dimensional law $B(\rho)$, our simulation apparently neglects the influence of the velocity field on the magnetic field amplification. Indeed, B should be a multidimensional function that depends on ρ as well as on the velocity field in order to take into account dynamo and shear effects. The three models alluded to earlier do actually account for these effects up to some extent, as they reproduce the characteristic features obtained in the numerical simulations that include dynamo and shear effects. The choice of a random orientation of the magnetic field in each coherence cell also neglects the influence of large-scale motions. Simulations which follow explicitly the magnetic field indicate that this latter tends to be aligned with the principal directions of large-scale structure, i.e., the axis of the filament for example [26]. However, one should note that the simulations of Refs. [19,21,26] assume an initial magnetic field with infinite coherence length, so that the final coherence length of the final magnetic field along the axis of the filament equals the length of the filament (see Fig. 4 of Ref. [26] for an illustration of this effect). This of course is unrealistic (unless one assumes an

acausal origin for B) since the coherence length of the magnetic field should not exceed $\sim$1 Mpc, the typical turn-around time of an intergalactic eddy of this size being comparable to the age of the Universe [27,28].

In contrast, our simulation presents the advantage of simulating this multiple field reversal along the filament. The alignment of the magnetic field direction along the filament should take place if the coherence length is larger than the transverse size of the filament (more exactly the typical scale height of the density gradient). If, as is more likely, the coherence length is smaller, then the compression is similar to planar collapse as far as the magnetic field in a cell is concerned, hence the field becomes aligned transversely to the density gradient, and not necessarily along the filament axis. Our method offers the means to include this effect but we leave this investigation to future work for simplicity.

A last point concerning the distribution of the magnetic field in the intergalactic medium is related to its origin. The simulations of Refs. [19,21,26] set the initial conditions at high redshift and ignore other sources of magnetic pollution of the intergalactic medium (see Ref. [16] for a review on the origin of cosmic magnetic fields), such as galactic outflows, active galactic nuclei pollution [29–31], the amplification of magnetic fields in accretion shocks of large-scale structure (except Ref. [21] which uses a model of Biermann battery effects), turbulent amplification in the IGM [32], etc. These sources should influence the transport of high energy cosmic rays in two ways: by modifying the relationship between the volume averaged $\langle B \rangle$ and the value observed in cluster cores, and by adding additional scattering centers which have been omitted in these simulations. Our simulation technique offers the freedom to include such localized pollution effects in a simple and efficient way: one could include these highly magnetized regions in our simulation cube by sampling them according to the local matter density. For the sake of simplicity, in a first step we ignore these additional sources and postpone their study to further work. This choice is conservative in so far as the inclusion of localized regions of enhanced magnetic field would tend to amplify the magnitude of the low energy cutoff, all things being equal.

Finally, our simulation assumes for simplicity that the coherence length l_c is uniform in space, whereas it is likely to evolve as a function of the density and velocity fields. However, this brings in additional parameters which enlarge the parameter space. We believe that at this stage, it is more reasonable to study the influence of l_c by performing different runs with different values of l_c and comparing the results. Furthermore, the actual value l_c is intimately related to the origin of the magnetic field (which sets the initial l_c) as well as to the velocity fields which distort the field during the evolution, in particular, with the upbringing of MHD turbulence. Here as well, it should be clear that no simulation can claim to simulate these various effects with accuracy.

The issue of turbulence in the IGM is delicate, because the Reynolds number in the intergalactic medium may take large or moderate values depending on the environment. For turbulent excitation on a length scale L at velocity v, this Reynolds number reads [33]:

$$\mathcal{R}\, e \simeq 10^5 \left(\frac{L}{1\ \mathrm{Mpc}}\right)\left(\frac{v}{300\ \mathrm{km/s}}\right)\left(\frac{T}{10^5\ \mathrm{K}}\right)^{-5/2}\left(\frac{\rho}{\langle\rho\rangle}\right). \quad (6)$$

Turbulence is thus probably fully developed in most of the IGM, except in the high temperature regions representative of clusters of galaxies. In these regions of high kinematic viscosity, the shape and extent of the inertial range of turbulence is rather complex, and most likely influenced by the strong magnetic field, see Ref. [34] for detailed discussions. Turbulence plays a fundamental role in the transport of charged particles as well as in the reshaping of the distribution of the magnetic field, but its incorporation in numerical simulations of the gas density is extremely complex. As the largest scale of the turbulence cannot exceed a few hundred kiloparsecs or a megaparsecs, taking into account just one or two decades of inertial range necessitates an unrealistically high resolution since the cube size must remain larger than the inhomogeneity scale $\sim$100 Mpc. In this respect, our simulations provide more flexibility because our transport scheme in the simulated magnetic field allows to simulate the influence of a turbulence spectrum down to scales well below r_L, see Appendix A.

The present simulation technique thus combines simplicity, efficiency with flexibility, and the approximations on which it rests appear reasonable in regards of the uncertainties surrounding the origin of extragalactic magnetic fields, the nature of MHD turbulence, and the properties of cosmic ray transport in such turbulence. Most importantly, its parametrized description allows us to test the influence of the various parameters on the results in contrast with most other works on this topic.

III. RESULTS

The following results were obtained by computing the trajectories of 10^3 protons in inhomogeneous magnetic fields mapped according to four models, for many sets of energies E, magnetic field characteristic values B_0 and coherence lengths l_c. We will label in what follows "models 1–3" our modeling of $B(\rho)$ presented in Eqs. (4) and (5). We add to these models a last one (model 4) for which $B \propto \rho^{2/3}$ and the level of turbulence $\eta = \langle \delta B^2 \rangle / \langle B^2 \rangle \ll 1$, where δB is the inhomogeneous perturbation component of B (defined such as: $B = \langle B \rangle + \delta B$).

Though B_0 and $\langle B \rangle$ have quite similar numerical values, they are not strictly equal (they differ approximately by a factor 1.5). $\langle B \rangle$ represents the volume averaged magnetic field and B_0 is the proportionality factor in models (1–4), so that $B = B_0 \times f(\rho)$, where $f(\rho)$ is dimensionless.

The particles are emitted from 10 different sources chosen randomly among regions of high baryonic density. A detailed description of our code is given in Appendix A.

We first spot the existence of a magnetic horizon using the isotropic collapse magnetic field model [Eq. (4)]. We then move on to other models, calculate their resulting propagation spectra and study the influence of our two main parameters: B_0 and l_c.

A. Existence of a magnetic horizon

Figure 2 shows two examples of proton trajectories (solid line: $E = 10^{17}$ eV, dotted line: $E = 10^{19}$ eV) in a slice of simulated universe. The characteristic magnetic field is taken as $B_0 = 1$ nG and the coherence length as $l_c = 100$ kpc.

Obviously the particles at $E = 10^{19}$ eV and $E = 10^{17}$ eV evolve completely differently: the former travel in a rectilinear regime without being affected by changes in density, whereas the latter experience a diffusive propagation. Taking a closer look at the diffusive trajectory, one notices the expected intuitive correlation between the fluffiness of the trajectory and the clustered regions.

Figure 3 illustrates these comments in a more quantitative way. It shows the root mean square of the distance of 10^3 particles to their source after one Hubble time (13.9 Gyr) as a function of their energy, for a characteristic magnetic field $B_0 = 2$ nG and a coherence length $l_c = 300$ kpc. Our results are no longer valid beyond the dot-

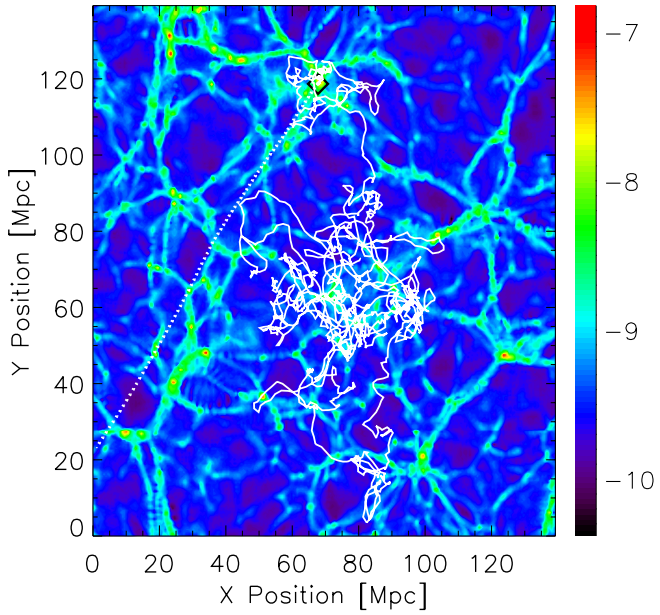

FIG. 2 (color online). Trajectories of protons of different energies (solid line: $E = 10^{17}$ eV, dotted line: $E = 10^{19}$ eV) in a slice of simulated universe. The characteristic magnetic field is taken as $B_0 = 1$ nG and the coherence length as $l_c = 100$ kpc. The colorbar on the side indicates the intensity of the magnetic field (in log).

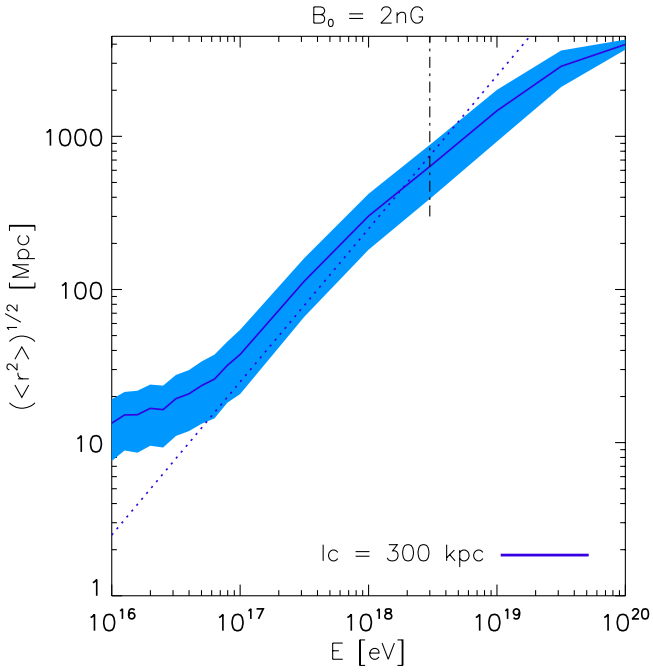

FIG. 3 (color online). Root mean square of the distance of 10^3 particles to their source after one Hubble time ($t_H \sim 13.9$ Gyr) as a function of their energy, for $B_0 = 2$ nG and $l_c = 300$ kpc. The solid line represents the root mean square of the distance and the surrounding color band its variance. The dotted line shows the values obtained from analytical calculations in a homogeneous magnetic field [Eq. (9)] and the dot-dashed line the threshold energy above which the energy loss time becomes $\lesssim t_H/2$.

dashed line which represents the threshold energy above which the energy loss time becomes $\lesssim t_H/2$, as our simulations do not compute energy losses.

The first striking remark is that particles of energy below $E \sim 3 \times 10^{17}$ eV cannot travel farther than a distance of a hundred megaparsecs from their sources. This corroborates the scenario of Refs. [8,9] on the existence of a magnetic horizon, and extends it to the case of a inhomogeneous magnetic field.

The curve presented in Fig. 3 comprises three distinct parts: a diffusive part with a slope of $\sim 1/6$, a semidiffusive part (slope ~ 1) and a quasirectilinear part with a slope tending towards zero. These trends can be naturally explained by analyzing the propagation regimes at different energies, in *homogeneous* magnetic fields.

The quantity $\langle r^2 \rangle^{1/2}$ plotted in Fig. 3 can be easily related to the diffusion coefficient through the equation

$$\langle r^2 \rangle = 2Dt_H, \tag{7}$$

where t_H is the Hubble time and D the diffusion coefficient. This equation follows straightly from the definition of $D \equiv \langle \Delta x^2 \rangle / 2\Delta t$, where Δx represents the displacement during the time interval Δt. Thus our computation of D in

our simulations has a direct influence on the shape of the curve observed in Fig. 3.

As explained in Appendix A, our diffusion coefficient is calculated following the results of Casse *et al.* [18]. It accounts for both diffusive ($r_L \ll l_c$) and semidiffusive ($r_L > l_c$) regimes. In the case of a diffusive regime, Eq. (A2) becomes

$$D \propto r_L^{1/3} l_c^{2/3}, \tag{8}$$

which corresponds to the standard Kolmogorov diffusion regime. Besides, when the Larmor radius r_L is somewhat greater than the coherence length of the magnetic field, we have the well-known dependence

$$D \propto r_L^2 l_c^{-1}. \tag{9}$$

Knowing that $r_L \propto EB^{-1}$, we get from (8) and (9): $\langle r^2 \rangle^{1/2} \propto E^{1/6}$ at low energies and $\langle r^2 \rangle^{1/2} \propto E$ for higher energies.

It is quite surprising that these slopes, expected for homogeneous magnetic fields, are also observed in our inhomogeneous simulations for the magnetic field model and the set of parameters presented in Fig. 3. We will show in the following section that this is not true for other models and parameters.

When we get to very high energy ($E \sim 10^{18.5}$), the slope of $\langle r^2 \rangle^{1/2}$ versus E gets weaker, as particles enter the quasirectilinear regime. Equation (7) is no longer valid as particles never reach the diffusion regime.

Another illustration of the existence of the magnetic horizon is presented in Fig. 4. The transmission factor is plotted as a function of particle energy for three distances to the source (dashed lines: 10 Mpc, solid lines: 100 Mpc, dotted lines: 300 Mpc). Given an initial source position, we propagate protons over one Hubble time. At a distance R from the source, we calculate the transmission factor by taking the ratio between the number of particles situated beyond R and the total number of particles that were emitted.

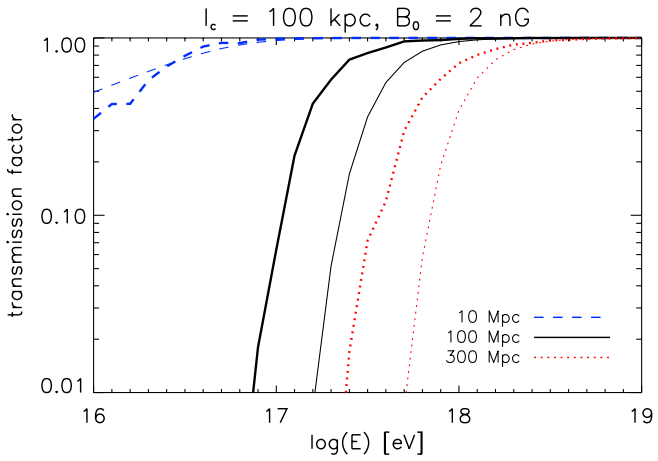

FIG. 4 (color online). Particle transmission factor at various distances from the source, as a function of particle energy. Thick lines are results from the simulation run with $B_0 = 2$ nG and $l_c = 100$ kpc. Thin lines represent the analytical transmission factor for a homogeneous magnetic field [Eq. (B3)].

Figure 4 clearly indicates the presence of a magnetic horizon: for energies below $\sim 2 \times 10^{17}$ eV, only half of the emitted particles reach a distance of 100 Mpc in a Hubble time. The cutoff energy is lower than for the case represented in Fig. 3 due to the lower value of l_c, as will be explained in Sec. III B.

Thin lines represent the analytical transmission factors calculated in Appendix B using the diffusion coefficient implemented in our code [Eq. (A2)], for the homogeneous case. For a given energy with a particular set of parameters, one can calculate the corresponding Larmor radius r_L and then D using (A2). It is then easy to obtain $\hat{R}$ and calculate T using (B3).

For the isotropic collapse model (model 1) and the represented parameters ($B_0 = 2$ nG, $l_c = 100$ kpc), there is a noticeable difference between the homogeneous and the inhomogeneous cases. The cutoff occurs at lower energy for the inhomogeneous case, probably due to voids that enable particles to travel farther.

The previous remark does not stand for a travelled distance of 10 Mpc [(blue) dashed lines]). On the contrary, the transmission factor in an inhomogeneous magnetic field is lower than in the homogeneous case. This is due to the influence of the dense environment of the source where particles were emitted. On a small scale of 10 Mpc, low energy particles have just escaped the high density region surrounding their source and cannot propagate as far as in the homogeneous case. The influence of the environment will be discussed in Sec. IV B.

B. Calculated spectra

In order to compare our results with observational data, we derive spectra from our simulations in the following way. Reference [8] has shown that the solution to the diffusion equation in an expanding universe, assuming a constant comoving distance between scattering centers, and limiting itself to energy losses by expansion (which is correct at energies below $\sim 10^{18.3}$ eV) takes the form

$$J_{\text{diff}} = \frac{c}{4\pi} \int \mathrm{d}t \sum_i \frac{e^{-r_i/(4\lambda^2)}}{(4\pi\lambda^2)^{3/2}} \frac{\mathrm{d}E_g(t,E)}{\mathrm{d}E} Q(E_g(t,E)). \tag{10}$$

This solution agrees with Ref. [35], which derives the general diffusion equation in an expanding universe and presents the solutions for various energy losses.

In Eq. (10) above, r_i represents the comoving distance to source i, $E_g(t, E)$ the required energy at time t in order to have an energy E at t_0 given the energy losses, $Q(E_g)$ the emission rate per source at energy E_g and λ the comoving "path length." λ is defined as

$$\lambda^2 = \int_{t_e}^{t_0} \frac{\mathrm{d}t}{a(t)} D\left[\frac{a_e E_e}{a(t)}\right], \tag{11}$$

where a_e is the scale factor at emission and D the diffusion coefficient. Physically, λ represents the typical distance travelled by diffusion, accounting for energy losses.

In order to calculate λ, we first study the dependence of D on E, B_0, and l_c using our simulations. We find that each set of parameters corresponds to a different function $D(E, B_0, l_c)$. We then parametrize the evolution of the magnetic configuration as done by Berezinsky and Gazizov [36], as

$$l_c(z) = l_c(1+z) \quad \text{and} \quad B_0(z) = B_0(1+z)^{2-m}, \tag{12}$$

where m characterizes the MHD amplification of the field. For simplicity, we set m to 0 in our calculations. This toy model corresponds to a constant comoving distance between scattering centers and ignores magnetic field amplification during structure formation. In this way, we obtain the required dependence of D over t and thus the function $D[a_e E_e/a(t)]$.

The function $\mathrm{d}E_g(t, E)/\mathrm{d}E$ is calculated by integrating the energy losses, following the calculations of Berezinsky *et al.* [1]. The injection spectrum extends from 10^{16} eV to $E_{\max} = 10^{20}$ eV. The function $Q(E_g) = K(E_g/E_{\max})^{-\gamma}$ gives the emission rate per source at energy E_g, K being a normalization factor such that $\int \mathrm{d}E E Q(E) = L$, with L the total luminosity, which is assumed to scale as the cosmic star formation rate from Ref. [37]. We will assume in our calculation a spectral index of $\gamma = 2.6$. In any case, it should be pointed out that the choice of the star formation rate has little influence on our spectra, since the effects of the magnetic horizon dominates those of the star formation history on the low energy part of the spectrum.

At higher energies, when the comoving light cone distance $r(t) = \int_t^{t_0} \mathrm{d}t'/a(t')$ becomes smaller than $\lambda(t, E)$, the propagation is no longer diffusive and enters the rectilinear regime. In this case, the propagated spectrum is given by:

$$J_{\mathrm{rect}}(E) = \frac{c}{4\pi} \sum_i \frac{1}{4\pi r_i^2} \frac{1}{1+z_i} \frac{\mathrm{d}E_g(t_i, E)}{\mathrm{d}E} Q(E_g(t_i, E)), \tag{13}$$

where t_i is related to r_i by $r_i = \int_t^{t_0} \mathrm{d}t'/a(t')$, r_i, and z_i denoting the comoving distance and redshift of the ith source. The factor $1/(1+z_i)$ was omitted in Ref. [8], but it has no influence whatsoever as $z \ll 1$ when the rectilinear regime is reached.

Figure 5 presents the influence of the $B(\rho)$ models and of parameters B_0 and l_c on the magnetic cutoff. Only the diffusive part of the spectra is represented there and the falloff of the curve around $\sim 10^{18}$ eV corresponds to the transition between the diffusive and rectilinear propagation regimes. We assume continuously emitting sources with density $n_s = 10^{-5}$ Mpc^{-3} and plot the median spectrum obtained over 100 realizations of the source locations. For each realization, the location of the first hundred sources were uniformly sampled. For farther sources, the continuous source approximation is valid and it was used numerically.

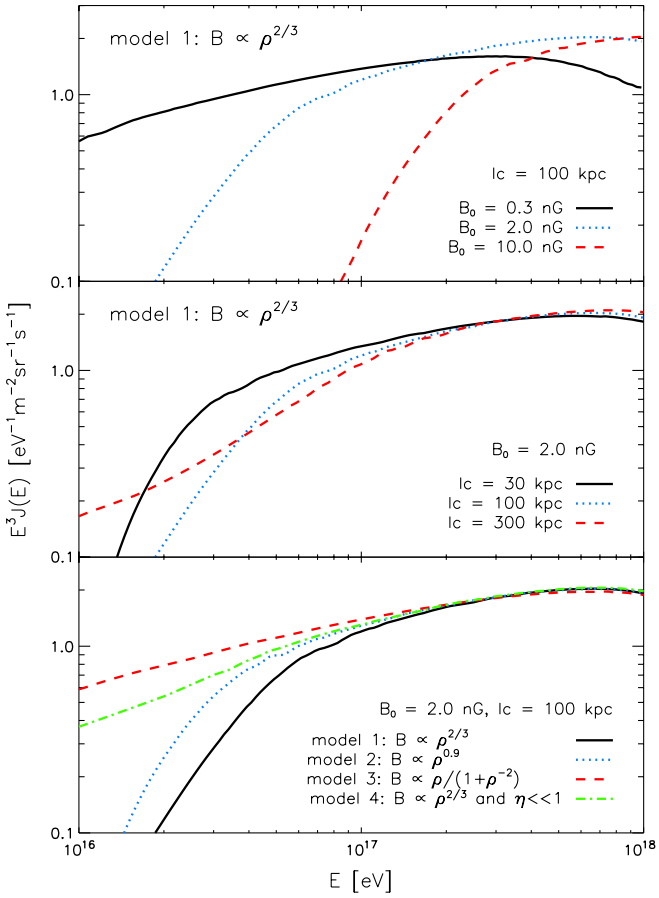

FIG. 5 (color online). *Upper panel*: influence of B_0 on the spectra for $l_c = 100$ kpc and model 1. *Middle panel*: influence of l_c on the spectra for a fixed value of $B_0 = 2$ nG and for model 1. *Lower panel*: influence of dependence of B over ρ on spectra (models 1–4), for fixed values of $B_0 = 2$ nG and $l_c = 100$ kpc.

The upper panel shows the intuitive result that the greater the mean magnetic field, the steeper the cutoff. Of course this law is not restricted to model 1 but is also valid for models 2–4.

The middle panel shows interesting features that are in agreement with Eqs. (8) and (9). For a fixed value of B_0, for low energies, particles are in the diffusive regime [see Eq. (8)] and $\langle r^2 \rangle$ scales with the coherence length as $l_c^{2/3}$. For higher energies particles are in the semidiffusive regime [see Eq. (9)] and $\langle r^2 \rangle \propto l_c^{-1}$. In other words, the spectrum cuts off more steeply for lower values of l_c for low energies and for greater values of l_c for high energies. This can be seen on Fig. 5: for $l_c = 300$ kpc, the spectrum cuts off at high energy but the slope is shallow for low energies, whereas for $l_c = 30$ kpc, the slope is steep at low energies but the cutoff starts at lower energies.

In view of these trends, one will have to find a good compromise in order to obtain satisfactory fits to the observational spectra.

The lower panel illustrates the shape of the cutoff for the four models previously described. Models 3 and 4 present a much shallower slope compared to models 1 and 2. The almost total absence of magnetic field in the large-scale structure voids for model 3 and the cancellation of turbulence in model 4 can explain this. We also notice that model 1 which has a higher magnetic field intensity in the voids cuts off in a steeper way than for model 2.

For a better understanding of the trends seen in the lower panel of Fig. 5, we plot in Fig. 6 the root mean square of the distance of 10^3 particles to their source after one Hubble time as a function of their energy, as in Fig. 3, for models 1–4. Variances have the same width for all models; we did not represent them for clarity. As already mentioned, the functions represented in this figure are closely related to the diffusion coefficient D [see Eq. (7)], which is required to calculate the spectra in the diffusive regime.

In Fig. 7 we present the total spectra (galactic + extragalactic) compared to the data, for our parameter fit for each model. As for Fig. 5, we draw the median spectrum (dot-dashed line) obtained over 100 realizations of the source locations. The upper and lower dotted curves show the 75th and 25th percentiles around this prediction, meaning that only 25% of spectra are higher or lower, respectively, than indicated by the curves. This uncertainty is related to the location of the closest sources. As explained in Ref. [8], we draw a straight dashed line in the region

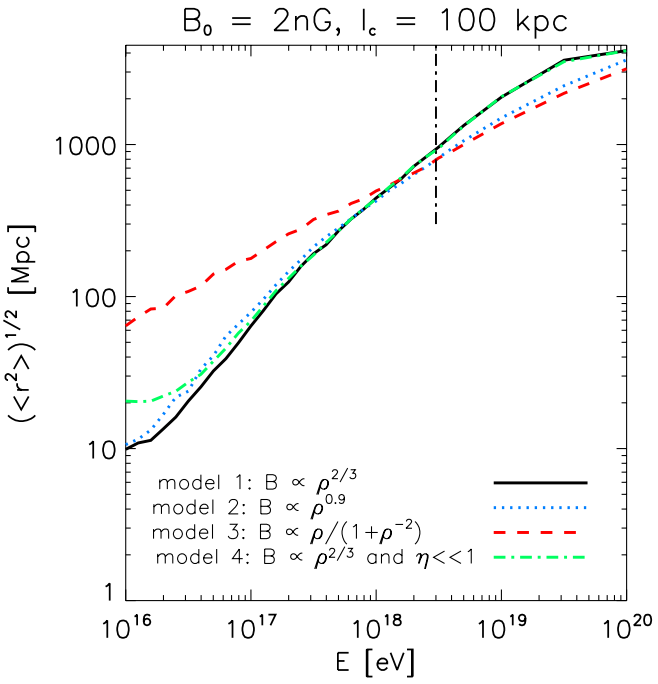

FIG. 6 (color online). Same as Fig. 3, for $B_0 = 2$ nG and $l_c = 100$ kpc, for models 1–4. Variances are not represented.

slightly above 10^{18} eV, where the propagation is neither rectilinear nor diffusive (see Ref. [8] for more details on this transition zone).

The galactic cosmic ray component is modeled as follows. Supernovae are accepted as standard acceleration sites, yet it is notoriously difficult to explain acceleration up to maximal energy 10^{18} eV. Thus it is assumed that the knee sets the maximal acceleration energy for galactic cosmic rays: in this conservative model, the spectrum of species i with charge Z takes the form $j_Z(E) \simeq (E/E_Z)^{-\gamma_i} \exp(-E/E_Z)$, with $\gamma_i \sim 2.4$–2.7, a species dependent spectral index, $E_Z \simeq Z \times 2 \times 10^{15}$ eV [38]. The total galactic component is obtained as the sum of elemental spectra, each adjusted to KASKADE data as described in Ref [8].

We use the data of six major experiments that measured the cosmic ray fluxes in our regions of interest: KASKADE (2004 data), with an energy range going from 10^{15} to 10^{17} eV [38], Akeno from 10^{15} to $10^{18.6}$ eV [39], AGASA from $10^{18.5}$ to $10^{20.5}$ eV [40], HiRes I and II from $10^{17.3}$ to 10^{20} eV [41] and Fly's Eyes from $10^{17.3}$ to 10^{20} eV [42]. We split these data in two sets in order to account for the discrepancy between HiRes and AGASA. This enables us to have two different normalizations for the extragalactic flux on the left and right panels. The normalization of KASKADE data remains the same for both sets.

Four main points emerge from Fig. 7. *(i)* The second knee feature appears more or less clearly in the four models, but ultimately remains quite robust to model changes. *(ii)* However, again, the influence of the magnetic field intensity in voids is obvious: even with a source density of $n_s = 10^{-6}$ Mpc^{-3}, the goodness of fit of model 3 with the observed spectra is only marginal. This situation is clearly improved in the other models, especially if we consider the uncertainty on the position of the closest sources. *(iii)* One might also notice that this last element has a considerable impact on the cutoff energy, much more than in the case of the homogeneous magnetic field of Ref. [8]. This is due to the presence of the diffusive regime at the low energy tail. One can indeed observe in Fig. 6 the flat diffusive locus at low energies for models 1 and 4. Phenomenologically, one understands that for these models, a slight change in the closest source distance can influence greatly the flux of low energy particles. *(iv)* Finally, comparing our plots for AGASA and HiRes data, we conclude that the fits are better for the latter. The higher slope above the second knee break point in the HiRes data as well as the gap of data between the KASCADE and HiRes ranges make the fitting easier.

One should emphasize, however, that the above fits were obtained by hand, not by any optimization procedure due to the computing time required to compute one spectrum. Therefore, the spectra shown above does not strictly speaking represent the best fit to the data. Furthermore, one

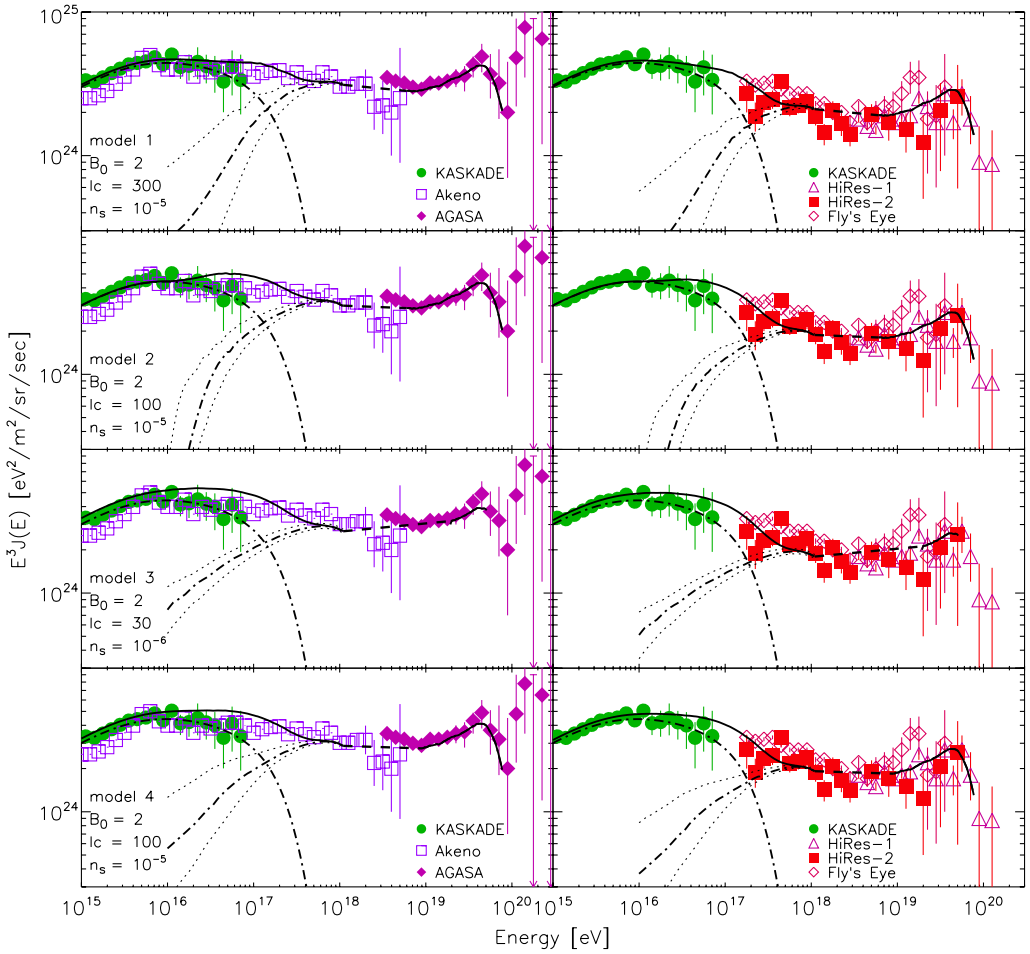

FIG. 7 (color online). Total spectra (galactic + extragalactic) compared to data. Each row corresponds to a model and a set of parameters. Caution: $n_s = 10^{-6}$ Mpc^{-3} for the third row. The left panels show KASKADE, Akeno, and AGASA data. The right panels show KASKADE, HiRes-1, HiRes-2, and Fly's Eyes data. Solid lines represents the median values of the total flux, dot-dashed lines the separate galactic and extragalactic components, and the dotted lines the upper 75th and lower 25th percentiles for the magnetic cutoff of the extragalactic flux.

should also exert some caution when comparing data sets from different experiments. In Fig. 7, we chose to plot separately the AGASA and HiRes data because of the well-known discrepancy, but one cannot exclude a discrepancy between the energy scales of KASCADE and HiRes for instance, which would shift one data set with respect to the other. Given all these uncertainties, the fits shown in Fig. 7 appear satisfactory, except maybe that of model 3 in which the cutoff always appears too mild.

IV. DISCUSSION

A. Current limitations

As already discussed in Sec. II, our simulations do not take into account several different features of extragalactic magnetic fields, both for the sake of simplicity and because they are in any case poorly understood and poorly constrained. We thus mentioned that our fields are related to the gas distribution according to three models [Eqs. (4) and (5)], which are one dimensional, that no magnetic source is included, and that the coherence length is assumed to be uniform in space.

Another point that should be underlined is that we propagate our particles in a static universe, represented by the final output (at $z = 0$) of a cosmological simulation. In other words, the magnetic fields do not evolve in time during our simulations. The Universe being more dilute at higher redshifts, the effects of inhomogeneous magnetic fields may be less important. A way of improving our results could be to propagate directly particles in an evolving magnetic field. Such a method would however be very time consuming and as explained in Sec. II, subject to too many uncertainties. One could also apply our semianalytical propagation method to a series of snapshots of the density of the Universe at various z. But again, one stumbles over our lack of knowledge about extragalactic magnetic fields: we have no hint of the evolution in time of the relation $B(\rho)$. Considering all these uncertainties, our restriction to a simple static universe thus appears reasonable.

Finally, we did not account for energy losses during the simulations which serve us to "measure" the diffusion coefficient, but included them in the calculation of the spectra presented in Sec. III B. For energies below $E \sim 10^{18}$ eV that are of interest to us in this paper, only expansion losses play a noticeable role (see [1]), at least at low redshift ($z < 1$). Above $\sim 10^{18}$ eV and for greater redshifts, energy losses by photopion and pair production are no longer negligible. Accounting for these energy losses should soften the low energy part of Fig. 3 if the magnetic field does not evolve strongly with redshift. Indeed, some of the particles at $E \sim 10^{16-17}$ eV actually result from higher energy particles that lost their energy. The greater distance travelled by these particles before losing their energy would tend to raise the rms of the distance to the source for low energy particles. Let us stress again that in order to model this effect, one would need to follow as well the evolution of the magnetic field with redshift.

B. Signatures

Firstly, we showed in Sec. III B that only some particular types of magnetic fields were able to reproduce the data, in the context of our study. Namely, for a source density of $n_s = 10^{-5}$ Mpc^{-3}, the voids of large-scale structures should have a certain level of magnetization, and $\langle B \rangle$ should be roughly comprised between 0.3 and 10 nG, 2 nG being an overall satisfactory average intensity. These numbers should be taken cautiously, remembering all the limitations and unknowns that affect these kind of simulations, as stated in the first two sections.

We calculated the Faraday rotation measure (RM) for our four magnetic field models with a characteristic magnetic field of $B_0 = 2$ nG. Having sampled 10^4 lines of sight in our simulation cube, we calculated the median of the RMs along them. For our models, the power laws of median (RM) versus the distance are steeper (slope ~ 1) than that expected for a homogeneous magnetic field, for which the integration of RM is equivalent to a simple random walk (slope $\sim 1/2$).

We find that at a cosmological distance of 1 Gpc, the median of our RMs is of order ~ 0.03 rad/m^2 for model 1 and of ~ 0.1 rad/m^2 for models 2 and 3. These values are consistent with the current observations of RMs that predict an upper limit of 5 rad/m^2 [13]. It should be remarked however that the RMs calculated here are subject to high variations according to the concentration of matter along the line of sight. Though the distribution of the RMs is sharply peaked around 0, with most of the RMs in the narrow interval of $[-0.5, 0.5]$ rad/m^2, we still find some punctual cases where the RM can diverge from 20 up to 2000 rad/m^2.

The use of a median value of RM enables us to get rid of the undesirable lines of sight that cross high density clusters and that induce these divergences. These few lines of sight have a dominant contribution especially if we calculate the variance or the root mean square of RM, leading to very high artificial values.

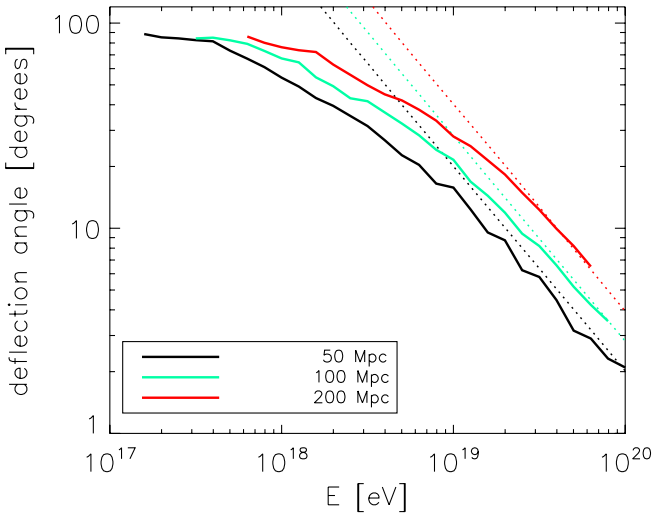

FIG. 8 (color online). Mean deflection angles at various distances from the source, as a function of particle energy, for model 1. Solid lines are the results of our simulation with $B_0 = 2$ nG, $l_c = 300$ kpc and using model 1 [Eq. (4)]. Dashed lines are the analytical values calculated in Ref. [43] [Eq. (14)].

Note that our rotation measures are again calculated for magnetic fields that do not evolve in time. Hence our median values can be considered as upper limits, as far as relatively low density regions are observed.

Mean particle deflection angles induced by the magnetic fields of model 1 are presented in Fig. 8. At a given distance from the source, we calculate the deflection angle between the arrival direction and the line of sight to the source. We stop computing the angles when the energy loss distance becomes greater than the linear travelled distance.

Our curves compare quite well to the analytical deflection angles calculated by Waxman and Miralda-Escudé [43] (dashed lines)

$$\langle \theta \rangle \simeq 0.8^\circ \left(\frac{E}{10^{20}\ \mathrm{eV}}\right)^{-1} \left(\frac{l_c}{1\ \mathrm{Mpc}}\right)^{1/2} \left(\frac{r}{10\ \mathrm{Mpc}}\right)^{1/2} \times \left(\frac{B}{10^{-9}\ \mathrm{G}}\right), \quad (14)$$

where r is the distance to the source. For all distances, the curves deviate from the analytical model at low energies, when diffusion becomes important, and saturate at 90°.

The deflections obtained for cosmological distances at high energy are quite moderate for model 1. We calculated that it is also the case for models 2 and 4 (deflections are slightly amplified in model 3). For a particle energy of 5×10^{19} eV and a magnetic field of $B_0 = 2$ nG and $l_c = 300$ kpc, we find that the deflection is of order $\sim 3^\circ$–5° at 100 Mpc for models 1 and 2, and of $\sim 8^\circ$ for model 3. These results are consistent with the observations of dou-

blets and triplets of events by recent experiments and leave room for doing cosmic ray astronomy. Our models would thus be in agreement with the detection of counterparts at energies around the Greisen-Zatsepin-Kuzmin cutoff.

Recently, a study related to the present work appeared, claiming that partial confinement in magnetic fields surrounding the source plays an important role in the cutoff at low energy [44]. This possibility had been put forward in Ref. [8], where it was further shown that the time of escape from the dense source environment could be non-negligible only in a rather contrived situation, since it requires $B \gtrsim 1\ \mu\mathrm{G}(l_c/10\ \mathrm{kpc})^{1/2}(L/100\ \mathrm{kpc})^{-1}$, with L the characteristic scale of the magnetic field spread around the source.

We do not find such a strong effect in our present simulations, where the time of confinement remains of order $\sim$1 Gyr for a particle of energy 10^{16} eV, or $\sim$300 Myr for a particle of energy 10^{17} eV. This effect obviously depends largely on the source environment, and on the location of the source. Ref. [44] samples the source locations according to the baryon density and therefore tends to favor high density (cluster) regions. Since the magnetic field in the simulations of Ref. [44] is already quite strong (see Fig. 1), this explains the magnitude of the effect. As noted in Ref. [8], the search for counterparts will allow to confirm or exclude this effect by studying the environment of the sources.

Ref. [44] also calculates spectra for inhomogeneous magnetic fields. However, unlike in our work, Ref. [44] does not account for the evolution of the magnetic field due to expansion during the propagation.

Nevertheless it is interesting that Ref. [44] finds the spectrum to maintain its ''universal'' shape in the region of moderate energies, where the transition between the diffusive and the rectilinear regimes occurs. This is one region which we cannot probe using the semianalytical technique of spectrum reconstruction used in the present work; the results of Ref. [44] justify our interpolation of the spectrum in this region.

V. CONCLUSION

We developed a new method combining an efficient propagation scheme and a simple recipe to build semi-realistic magnetic field distributions. We map the magnetic field following the baryon density distribution according to three different models and propagate particles from cell to cell, taking into account the inner turbulence of each cell, as well as its global magnetic intensity. This method is much faster than classical trajectory integrations.

Under the assumption that the emergence of the extragalactic component occurs at the second knee, we demonstrated that it was possible to give rough limits for some key parameters $(\langle B\rangle, l_c)$, by studying their effects on the magnetic horizon.

For our models assuming isotropic or anisotropic collapse, with or without turbulence (models 1, 2, and 4 described in Secs. II and III), we find that our calculated spectra fit the data satisfactorily. Numerically, for a source density of $n_s = 10^{-5}\ \mathrm{cm}^{-3}$ we find that an average magnetic field $\langle B\rangle = 2$ nG is a reasonable value for the three models cited above, and coherence lengths of 100 kpc (for models 2 and 4) up to 300 kpc (model 1) provide a good agreement with the data. These numbers should still be taken cautiously, remembering the limitations discussed throughout this paper.

We showed that the validity of this scenario depends on other parameters (relative normalization of data sets, source density) but eventually, the strongest constraint comes from the rate of magnetic enrichment of the low density intergalactic medium (voids). We saw indeed that model 3, which simulates a volume with unmagnetized voids has a marginal goodness of fit with the observed spectra, even with a low source density.

Ultimately, therefore, the success of this scenario for the transition between the galactic and extragalactic cosmic ray components depends on the very origin of intergalactic magnetic fields, and on whether the voids of large-scale structures have remained pristine or not. Interestingly, this question is related to the ongoing debate on the enrichment of the underdense intergalactic medium in metals, since galactic winds carrying metals also carry significant magnetic fields. Detailed studies of the intergalactic medium as well as progress on extragalactic magnetic fields in the coming decade will shed light on this issue.

ACKNOWLEDGMENTS

We would like to thank Stéphane Colombi who provided us with the hydrodynamical simulation outputs and Christophe Pichon for valuable discussions.

APPENDIX A: NUMERICAL TECHNIQUES

1. Setting up the magnetic field

Our basic assumption is that the magnetic field and the matter density have a similar spatial distribution at large scales. For the reasons detailed in Sec. II, we map the magnetic field following four models [Eqs. (4) and (5)]. The parameter B_0 mentioned along this paper refers to the proportionality factor of Eqs. (4) and (5) and indicates the characteristic intensity of the field.

We calculate our magnetic field by applying these formulas to a three dimensional dark matter overdensity map (at redshift $z = 0$) generated by the hydrodynamical code RAMSES [23]. This cosmological simulation was based on a the ΛCDM model that assumes a flat, low density universe, with $\Omega_m = 0.3$, $\Omega_\Lambda = 0.7$, and Hubble constant $h \equiv H_0/(100\ \mathrm{km/s/Mpc}) = 0.7$. It models a 200 Mpc/$h$ comoving periodic cube split in 512^3 cells, where the dark matter overdensity is computed. We do not resolve struc-

tures below Jeans length, which implies that we can identify the computed dark matter distribution to a gas distribution.

While propagating our particles, the magnetic field at a given position is computed using the overdensity of the nearest grid point.

2. Particle propagation

For each set of parameters, we propagate 10^3 protons emitted from 10 different sources. The positions of the sources are chosen as follows: we first select the grid points in our cube that have an overdensity $\tilde{\rho} > 10$. Smoothed over our grid of 512^3 cells for 200^3 Mpc^3, overdensities of $\sim 10^3$ (minimum density of galaxies) would indeed correspond to overdensities of ~ 10. Thus the selected regions have a good probability of belonging to massive halos. We randomly choose ten grid points among this subset and label them as the initial positions of our particles. The initial direction of the impulsion of a particle is also drawn randomly.

a. Computing the trajectory

Solving the equation of motion for each particle during an entire Hubble time using a Runge-Kutta method can be very time consuming. An alternative method consists in assuming that a proton travels through adjacent spheres of diameter l_c, in which the magnetic field has a certain level of turbulence (see Fig. 9). We calculate analytically the time of escape from each sphere and sample the deflection angle of the particle after each sphere from a normal law where the mean deflection m and its variance s depend on the Larmor radius of the particle. This sphere-crossing method is much faster than a direct integration of the trajectory. It also enables us to take into account the low level turbulence for scales smaller than l_c.

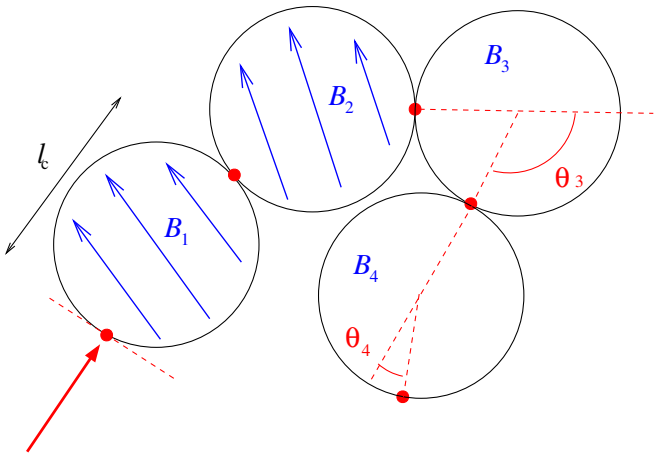

FIG. 9 (color online). Sketch of particle propagation in magnetic fields as modeled in our simulations. Particles enter spheres of diameter l_c along a radial direction and escape at calculated positions (marked with red dots). A global magnetic field intensity, that can be related to the largest scale of turbulence, is associated to each sphere (labeled B_i, with $B_3 > B_4$). Turbulence is taken in account inside each sphere through the calculation of the escape time and position. In this figure, $\cos\theta_3$ is sampled from a normal law with a large variance and $\cos\theta_4$ with a smaller variance.

A particle can cross a sphere in two extreme ways: either $p = r_L/l_c \gg 1$ and the particle goes nearly straight through the sphere, or $p \ll 1$ and it wanders in the sphere for some time. In this latter case, the time spent in the sphere $\tau_1 \simeq l_c/c$.

In the Kolmogorov regime in which the diffusion length $l_{\rm scatt} \sim r_L^{1/3} l_c^{2/3}$ with $r_L \ll l_c$, one always has $l_{\rm scatt} \leq l_c$ hence the particle enters the diffusive regime in the sphere before exiting. The time spent in the sphere then depends on the diffusion coefficient D.

On average, a particle diffusing through the sphere travels a *linear* distance $l_c/\sqrt{2}$, so that the time of escape reads

$$\tau_2 = \frac{l_c^2}{4D}. \tag{A1}$$

D is computed according to the results of Casse *et al.* [18], who performed Monte Carlo simulations of particle propagation in stochastic magnetic fields to measure the spatial diffusion coefficients. Their data for full turbulence can be fit by the approximate relation

$$D = 1.2 r_L c \left(\frac{r_L}{l_c} + 0.1 \left(\frac{r_L}{l_c} \right)^{-2/3} \right). \tag{A2}$$

We use this formula in our code to calculate τ.

b. Deflection angle calculation

Our spheres are located so that the particle always enters radially. The deflection angle due to the crossing of a sphere is calculated with respect to this entering direction (see Fig. 9).

The cosine of the deflection angle $\cos\theta$ varies according to the rigidity $p = r_L/l_c$. For $p \ll 1$ the particle is in a diffusive regime, which implies that $\cos\theta$ has a uniform distribution over $[-1, 1]$. For the other extreme case, namely $p \gg 1$, $\cos\theta$ can be sampled from a normal law of mean m and variance s.

In order to identify the functions $m = m(p)$ and $s = s(p)$ in the quasirectilinear regime, we integrated the trajectories of 10^4 particles in a sphere, using a Runge-Kutta method, for values of p ranging from 2 to 100. This gives us a trend for the mean deflection angle $\langle\theta\rangle$ and its variance $\delta\theta$.

Then, in our simulations, we use the calculated probability law given by $m(p)$ and $s(p)$ in order to draw the direction of exit, and we move the clock forward by the time spent in the sphere.

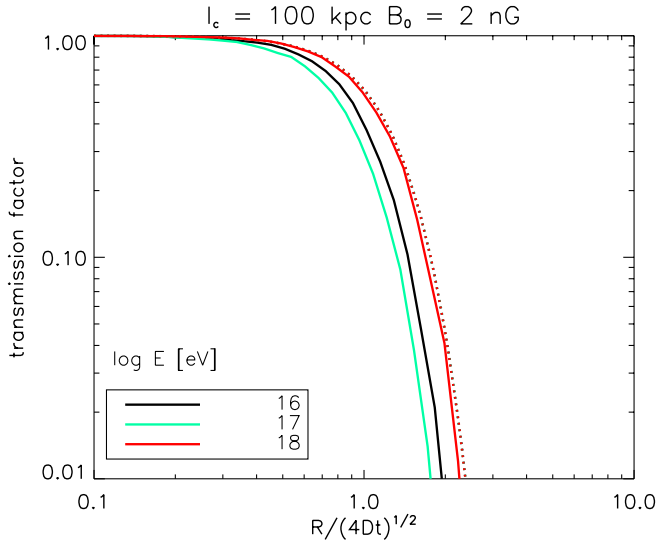

FIG. 10 (color online). Fraction of particles located at a linear distance greater than R after one Hubble time in a homogeneous magnetic field, as a function of $\hat{R} = R/\sqrt{4Dt}$ as defined in (B4), for various rigidities $p = r_L/l_c$. Solid lines are results from our simulations and dotted lines the analytical expression calculated in Appendix B.

c. Checking the validity of our code in a homogeneous case

Our code was checked on a broad range of parameters in the analytically calculable homogeneous case, i.e., we compared the numerical simulations using the above sphere-crossing trajectories and a magnetic field strength equal in each sphere with the analytical results for full turbulence and homogeneous magnetic power. We did obtain through the numerical calculations the expected slopes of 1/6 and 1 for Fig. 3 as predicted by the analytical calculations. The transmission factors also fit nearly exactly those calculated in Eq. (B3), see Fig. 10.

APPENDIX B: TRANSMISSION FACTOR FOR DIFFUSION IN HOMOGENEOUS SPACE

We calculate in this section the fraction of particles that are located at a linear distance greater than R at a given time t, in a diffusive propagation regime and in a homogeneous space. The density of particles at a position r and at time t can be written

$$n(r,t) = \frac{1}{(4\pi Dt)^{3/2}} \exp\left(-\frac{r^2}{4Dt}\right), \tag{B1}$$

where D is the diffusion coefficient. The fraction of particles beyond R at t can thus be obtained by the following integral:

$$T = \int_R^\infty 4\pi r^2 \mathrm{d}r \frac{1}{(4\pi Dt)^{3/2}} \exp\left(-\frac{r^2}{4Dt}\right). \tag{B2}$$

Integrating by parts, we obtain

$$T = \sqrt{\frac{2}{\pi}}\hat{R}\mathrm{e}^{\hat{R}^2/2} + \mathrm{erfc}\left(\frac{\hat{R}}{\sqrt{2}}\right), \tag{B3}$$

where

$$\mathrm{erfc}\,(x) = \frac{2}{\sqrt{\pi}} \int_x^\infty \mathrm{e}^{-u^2}\mathrm{d}u \quad \text{and} \quad \hat{R} \equiv \frac{R}{\sqrt{4Dt}}. \tag{B4}$$

[1] V. Berezinsky, A. Gazizov, and S. Grigorieva, Phys. Rev. D **74**, 043005 (2006).
[2] M. Nagano and A. Watson, Rev. Mod. Phys. **72**, 689 (2000).
[3] P.-O. Lagage and C. Cesarsky, Astron. Astrophys. **125**, L249 (1983).
[4] R. Budnik, B. Katz, A. MacFadyen, and E. Waxman, arXiv:astro-ph/0705.0041.
[5] A. R. Bell and S. G. Lucek, Mon. Not. R. Astron. Soc. **321**, 433 (2001).
[6] H. J. Völk and V. N. Zikashvilii, Astron. Astrophys. **417**, 807 (2004).
[7] H. Muraishi, S. Yanagita, and T. Yoshida, Prog. Theor. Phys. **113**, 721 (2005).
[8] M. Lemoine, Phys. Rev. D **71**, 083007 (2005).
[9] R. Aloisio and V. Berezinsky, Astrophys. J. **625**, 249 (2005).
[10] V. S. Berezinsky, S. I. Grigorieva, and B. I. Hnatyk, Astropart. Phys. **21**, 617 (2004).
[11] D. Allard, E. Parizot, A. V. Olinto, E. Khan, and S. Goriely, Astron. Astrophys. **443**, L29 (2005).
[12] D. Allard, E. Parizot, and A. V. Olinto, arXiv:astro-ph/0703633.
[13] P. P. Kronberg, Rep. Prog. Phys. **57**, 325 (1994).
[14] K. T. Kim, P. P. Kronberg, G. Giovannini, and T. Venturi, Nature (London) **341**, 720 (1989).
[15] B. M. Gaensler, R. Beck, and L. Feretti, New Astron. Rev. **48**, 1003 (2004).
[16] L. M. Widrow, Rev. Mod. Phys. **74**, 775 (2002).
[17] A. Lazarian, J. Cho, and H. Yan, arXiv:astro-ph/0211031.
[18] F. Casse, M. Lemoine, and G. Pelletier, Phys. Rev. D **65**, 023002 (2001).
[19] K. Dolag, D. Grasso, V. Springel, and I. Tkachev, J. Korean Astron. Soc. **37**, 427 (2004).
[20] K. Dolag, D. Grasso, V. Springel, and I. Tkachev, J. Cosmol. Astropart. Phys. 1 (2005) 9.
[21] G. Sigl, F. Miniati, and T. A. Enßlin, Phys. Rev. D **70**, 043007 (2004).
[22] J. Candia and E. Roulet, J. Cosmol. Astropart. Phys. 10 (2004) 007.

[23] R. Teyssier, Astron. Astrophys. **385**, 337 (2002).
[24] M. Bruni, R. Maarteens, and C. G. Tsagas, Mon. Not. R. Astron. Soc. **338**, 785 (2003).
[25] R. Schlickeiser and P. K. Shukla, Astrophys. J. **599**, L57 (2003).
[26] M. Brüggen, M. Ruszkowski, A. Simionescu, M. Hoeft, and C. Dalla Vecchia, Astrophys. J. **631**, L21 (2005).
[27] E. Waxman and J. Bahcall, Phys. Rev. D **59**, 023002 (1998).
[28] R. Aloisio and V. Berezinsky, Astrophys. J. **612**, 900 (2004).
[29] M. J. Rees and G. Setti, Nature (London) **219**, 127 (1968).
[30] S. R. Furlanetto and A. Loeb, Astrophys. J. **556**, 619 (2001).
[31] Gopal-Krishna and P. J. Wiita, Astrophys. J. **560**, L115 (2001).
[32] R. M. Kulsrud, R. Cen, J. P. Ostriker, and D. Ryu, Astrophys. J. **480**, 481 (1997).
[33] K. R. Lang, *Astrophysical Formulae*, Astronomy and Astrophysics Library (Springer, New York, 1999).
[34] A. A. Schekochihin and S. C. Cowley, Phys. Plasmas **13**, 056501 (2006).
[35] V. Berezinsky and A. Gazizov, Astrophys. J. **643**, 8 (2006).
[36] V. Berezinsky and A. Z. Gazizov, arXiv:astro-ph/0702102.
[37] V. Springel and L. Hernquist, Mon. Not. R. Astron. Soc. **339**, 289 (2003).
[38] K.-H. Kampert *et al.* (KASKADE Collaboration), Acta Phys. Pol. B **35**, 1799 (2004).
[39] M. Nagano *et al.* (Akeno Collaboration), J. Phys. G **18**, 423 (1992).
[40] M. Takeda *et al.* (AGASA Collaboration), Phys. Rev. Lett. **81**, 1163 (1998).
[41] R. U. Abbasi *et al.* (HiRes Collaboration), Phys. Rev. Lett. **92**, 151101 (2004).
[42] D. J. Bird *et al.* (Fly's Eyes Collaboration), Astrophys. J. **424**, 491 (1994).
[43] E. Waxman and J. Miralda-Escudé, Mon. Not. R. Astron. Soc. **472**, 89 (1996).
[44] G. Sigl, Phys. Rev. D **75**, 103001 (2007).